npj | 2D materials and applications

Article

Published in partnership with FCT NOVA with the support of E-MRS

https://doi.org/10.1038/s41699-024-00453-0

Exploration of the two-dimensional transition metal phosphide MoP_2 as anode for Na/K ion batteries

Junjie Jin & Udo Schwingenschlögl

Transition metal phosphides are regarded to be potential anode materials for alkali metal ion batteries with abundant availability of the constituent elements. However, the volume changes and resulting structure deterioration during the charge-discharge process are challenges. Using evolutionary search combined with ab initio calculations, we discover a dynamically, thermally, and mechanically stable MoP_2 monolayer, which turns out to be an excellent anode material for Na-ion batteries providing a high specific capacity of 339 mA h g^{-1}, low diffusion barrier of 0.12 eV, and low open-circuit voltage of 0.48 V. The volume expansion (125%) is found to be decisively smaller than in the case of black phosphorus (443%), for example.

Rechargeable Li-ion batteries are very successful in commercial energy storage, however, the scarcity (0.0017 wt% in earth's crust) and uneven geographical distribution of Li lead to high cost and cannot meet the quickly increasing demand[1–5]. Therefore, it is of great importance to explore battery systems based on abundant elements. Na-ion batteries (NIBs) and K-ion batteries (KIBs) are considered to be sustainable alternatives to Li-ion batteries because of the similarity of the physicochemical properties of Na/K to those of Li and the abundant availability of Na/K (2.3/1.5 wt% in earth's crust)[6–9]. While NIBs/KIBs share the operating mechanism with Li-ion batteries, the ionic radius of Na/K (1.02/1.38 Å) is much larger than that of Li (0.76 Å). Thus, most conventional anode materials of Li-ion batteries cannot be used for NIBs/KIBs[10]. For instance, graphite provides a Li specific capacity of 372 mA h g^{-1}, but only a Na/K specific capacity of 284/273 mA h g^{-1}[11–13]. Identifying high performance anode materials for NIBs/KIBs therefore is a critical issue.

Two-dimensional materials are promising options for the anode of NIBs/KIBs because they provide a large active surface and interlayer gaps to accommodate Na/K, enabling high energy density and high ion mobility[14–17]. Phosphorene, a well-known two-dimensional material, can form $(Na/K)_3P$ with a high specific capacity of 2596/1300 mA h g^{-1}[18,19]. However, the large ionic radius of Na/K causes a huge volume change during the charge-discharge process, leading to structure deterioration and rapid capacity decay[19]. Metal phosphides, on the other hand, can combine high electronic conductivity and small volume changes during the charge-discharge process with high specific capacities and suitable open-circuit voltages[20,21]. For this reason, we execute in the following an ab initio evolutionary search for metal phosphide monolayers suitable for application as anode of NIBs and KIBs.

Results and discussion

The relaxed structure of the MoP_2 monolayer is shown in Fig. 1a and the corresponding structural information is given in Table 1. There are four Mo atoms and eight P atoms in the unit cell, forming a 3.10 Å thick layer with the P atoms exposed at the surfaces, each P atom is bonded to one P and three Mo atoms, and each Mo atom is bonded to six P atoms. The Mo-P bond lengths of 2.43 and 2.47 Å are comparable to those in bulk MoP (2.48 Å)[22], orthorhombic MoP_2 (2.50 Å)[23], and two-dimensional structures with other Mo:P ratios[22,24]. The P-P bond length of 2.23 Å is comparable to those in black phosphorus (2.22 and 2.26 Å)[25]. The electron localization function is utilized to analyze the bonding character, with values of 1.0 and 0.5 representing localized and free electrons, respectively, whereas a value close to zero represents low electron density[26]. According to Fig. 1b, the electrons are more localized around the P atoms than around the Mo atoms. Bader charge analysis indicates that each Mo atom transfers 0.76 electrons to the P atoms. We obtain for the cohesive energy $E_{coh} = (4E_{Mo} + 8E_P - E_{MoP2})/12$, where E_{Mo}, E_P, and E_{MoP2} denote the total energies of a Mo atom, a P atom, and the MoP_2 monolayer (4 formula units per unit cell), respectively, a value of 4.79 eV per atom, which exceeds those of Cu_2P (3.21 eV per atom)[27], phosphorene (3.30 eV per atom)[28], BeP_2 (3.53 eV per atom)[29], FeP_3 (4.13 eV per atom)[30], and FeP_2 (4.39 eV per atom)[30]. Absence of negative phonon frequencies in Fig. 1c demonstrates dynamical stability of the MoP_2 monolayer. In addition, the results of our AIMD simulations, see Fig. 1d–h, exhibit no signs of structural disruption or phase transition at 300 K, demonstrating thermal stability. The structure is still stable at 1800 K but not at 1900 K, implying that the melting point of the MoP_2 monolayer falls into this range.

Physical Science and Engineering Division (PSE), King Abdullah University of Science and Technology (KAUST), Thuwal 23955-6900, Saudi Arabia.
e-mail: udo.schwingenschlogl@kaust.edu.sa

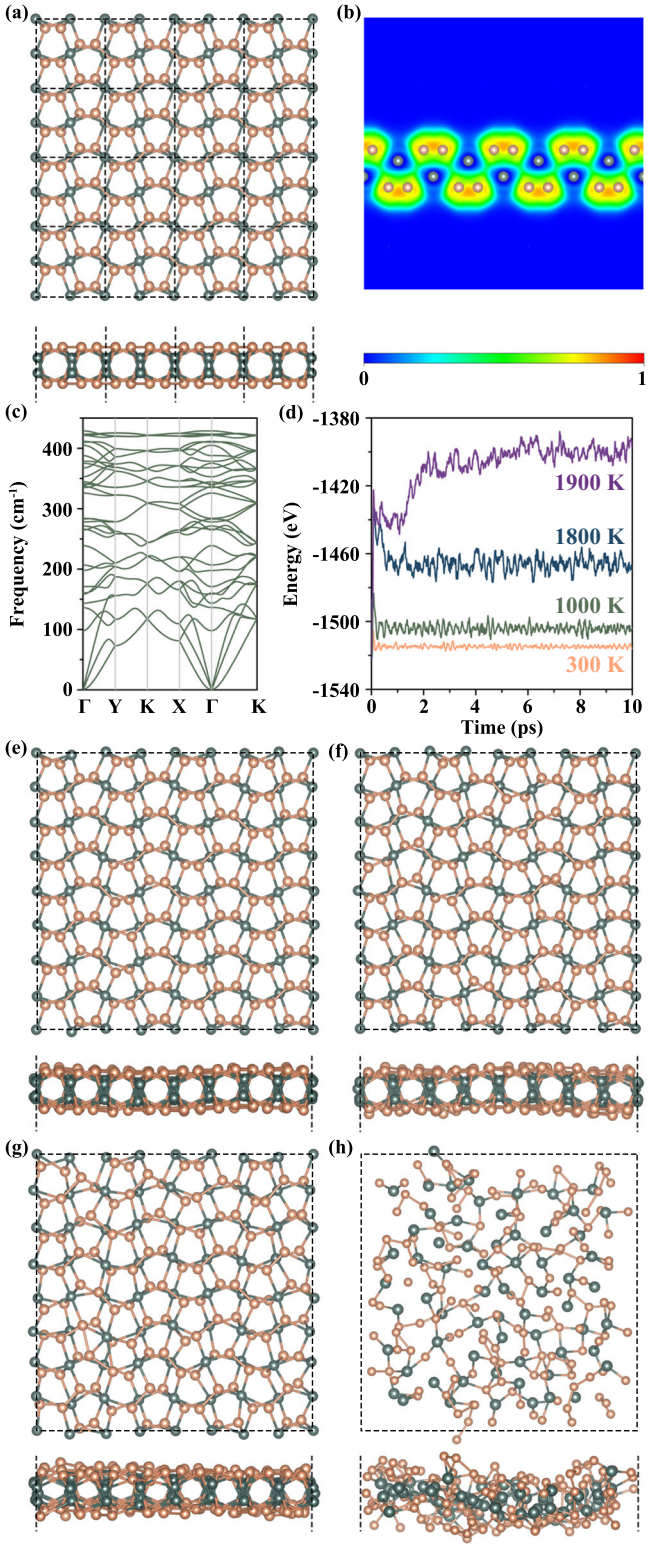

Fig. 1 | Structure and stability. a Top and side views of the MoP_2 monolayer (orange = P atoms, green = Mo atoms). The dashed lines mark the unit cell. **b** Electron localization function of the MoP_2 monolayer [(010) plane]. **c** Phonon spectrum of the MoP_2 monolayer. **d** Total energies during the AIMD simulations of the MoP_2 monolayer at 300, 1000, 1800, and 1900 K, and (**e**–**h**) top and side views of the corresponding final structures.

Table 1 | Structural information of the MoP_2 monolayer (space group Pcca, a = b = 5.80 Å, c = 25 Å)

atom	Wyckoff position	x	y	z
Mo1	8 f	0.500	0.000	0.042
Mo2	8 f	0.000	0.100	0.101
Mo3	8 f	0.500	0.500	0.101
Mo4	8 f	0.100	0.500	0.042
P1	8 f	0.364	0.364	0.000
P2	8 f	0.636	0.636	0.000
P3	8 f	0.864	0.636	0.142
P4	8 f	0.136	0.364	0.142
P5	8 f	0.364	0.864	0.142
P6	8 f	0.637	0.136	0.142
P7	8 f	0.864	0.136	0.000
P8	8 f	0.136	0.864	0.000

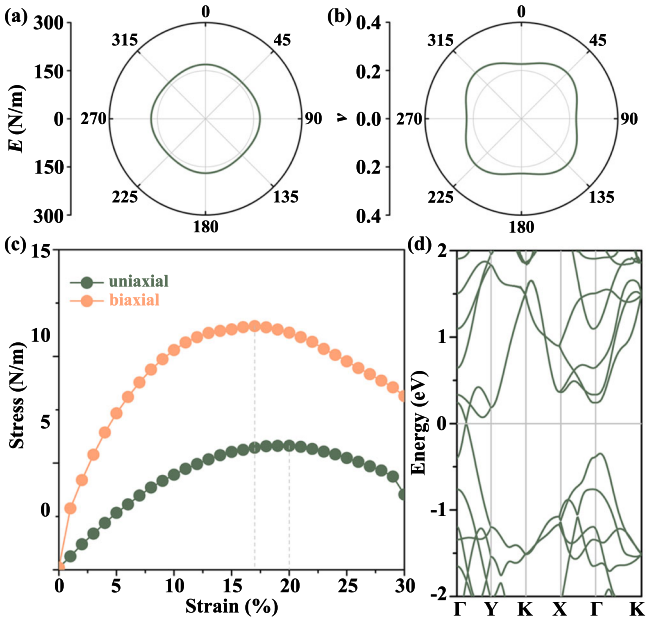

Fig. 2 | Mechanical and electronic properties. a Young's modulus. **b** Poisson's ratio. **c** Stress-strain curves (uniaxial and biaxial). and (**d**) electronic band structure of the MoP_2 monolayer.

The calculated elastic constants of the MoP_2 monolayer are $C_{11} = C_{22} = 178.7$ N m^{-1}, $C_{12} = 40.6$ N m^{-1}, and $C_{66} = 63.2$ N m^{-1}, obeying the mechanical stability criteria $C_{11}C_{22} - C_{12}^2 > 0$ and $C_{66} > 0$. We show in Fig. 2a the direction dependence (θ = angle with respect to the x-axis) of Young's modulus,

$$E(\theta) = \frac{C_{11}C_{22} - C_{12}^2}{C_{11}\sin^4\theta + [(C_{11}C_{22} - C_{12}^2)/C_{66} - 2C_{12}]\sin^2\theta\cos^2\theta + C_{22}\cos^4\theta}, \quad (1)$$

which characterizes the stiffness of a material, and in Fig. 2b the direction dependence of Poisson's ratio,

$$\nu(\theta) = \frac{C_{12}\sin^4\theta - [C_{11} + C_{22} - (C_{11}C_{22} - C_{12}^2)/C_{66}]\sin^2\theta\cos^2\theta + C_{12}\cos^4\theta}{C_{11}\sin^4\theta + [(C_{11}C_{22} - C_{12}^2)/C_{66} - 2C_{12}]\sin^2\theta\cos^2\theta + C_{22}\cos^4\theta}, \quad (2)$$

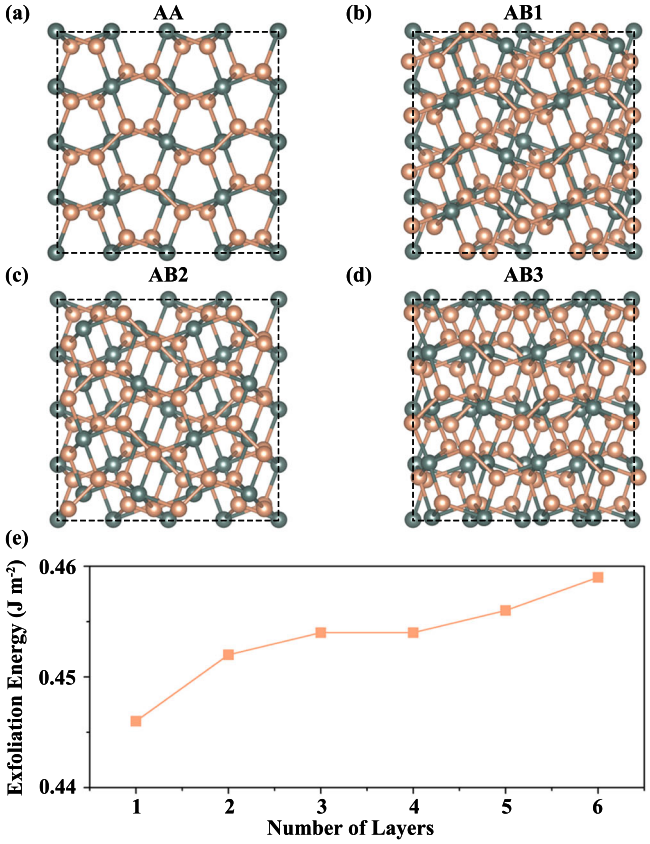

Fig. 3 | Stacking. a–d Relaxed structures of four possible stacking patterns of the MoP_2 bilayer. **e** Exfoliation energy per unit cell of a MoP_2 *n*-layer.

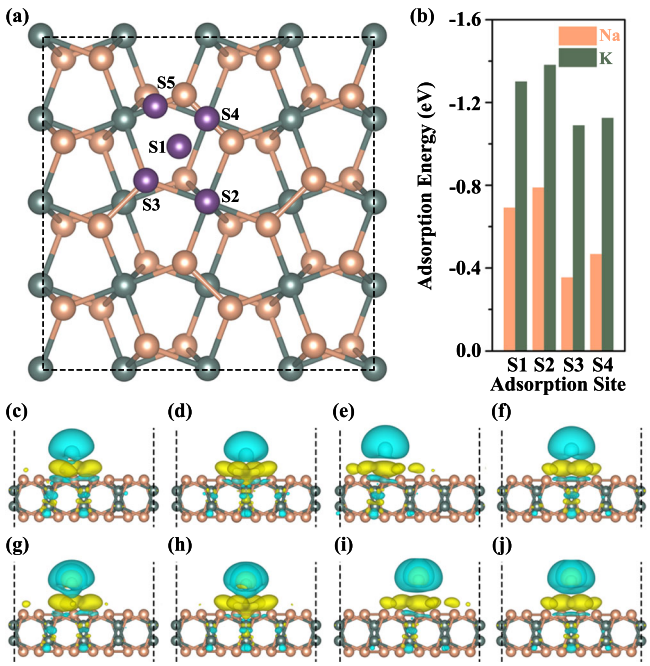

Fig. 4 | Adsorption. a Considered adsorption sites of Na/K on the MoP_2 monolayer. **b** Adsorption energies of Na/K on the MoP_2 monolayer. Na/K at the S5 site relaxes to the S2 site. Side views of the charge redistributions induced by **c–f** Na at the S1–S4 sites and (**g–j**) K at the S1–S4 sites. The cyan and yellow isosurfaces (isovalue = 0.008 electrons/Å^3) represent charge depletion and accumulation, respectively.

Table 2 | Adsorption energies (eV), adsorption heights (Å), and charge transfers (electrons) of Na/K on the MoP_2 monolayer at different sites

	site	E_{ad}	adsorption height	charge transfer
Na	S1	−0.69	2.17	0.85
	S2	−0.79	2.02	0.85
	S3	−0.35	2.49	0.87
	S4	−0.47	2.46	0.86
	S5	relaxes to the S2 site		
K	S1	−1.30	2.62	0.87
	S2	−1.38	2.48	0.87
	S3	−1.09	2.82	0.89
	S4	−1.12	2.83	0.88
	S5	relaxes to the S2 site		

which characterizes the response of a material to external load. According to Fig. 2a, the maximum of Young's modulus is 169.5 N m^{-1} at $\theta = 0°$, which is higher than those of phosphorene (92 N m^{-1} in the zigzag direction; 23 N m^{-1} in the armchair direction)[31] and MoS_2 (124 N m^{-1})[32], but smaller than that of graphene (334 N m^{-1})[32]. According to Fig. 2b, Poisson's ratio varies between 0.23 and 0.27. The fracture strain and strength are investigated by calculating the stress-strain curves shown in Fig. 2c. We find fracture strains of 20% (uniaxial) and 17% (biaxial) with corresponding fracture strengths of 5.8 and 11.4 N m^{-1}, which are comparable to those of phosphorene (27% and 10 N m^{-1} in the zigzag direction; 30% and 4 N m^{-1} in the armchair direction)[33] and MoS_2 (23% and 14.8 N m^{-1} biaxial)[34]. The electronic band structure in Fig. 2d shows several bands crossing the Fermi energy, reflecting excellent metallicity.

To determine the energetically favorable stacking pattern of the MoP_2 bilayer, we calculate the binding energy $E_b = (2E_{MoP2} - E_{bilayer})/N$ for the stacking patterns shown in Fig. 3a–d, where $E_{bilayer}$ is the total energy of the MoP_2 bilayer. With a binding energy of 39 meV per atom and an interlayer distance of 3.31 Å the AB2 stacking pattern is found to be energetically favorable. We further evaluate the *n*-layer exfoliation energy $E_{exf}(n) = (E_n - En/2)/S$, where E_n is the total energy of a MoP_2 *n*-layer in the vacuum, *E* is the total energy of a MoP_2 bilayer in the bulk, and *S* is the surface area. According to Fig. 3e, the exfoliation energy of the MoP_2 monolayer is 0.45 J m^{-2}, which is smaller than those of the InP_3 monolayer (1.08 J m^{-2})[35] and CaP_3 monolayer (1.30 J m^{-2})[36]. Consequently, the predicted MoP_2 monolayer is not only stable but it is likely that it can be prepared experimentally.

We use a 2 × 2 × 1 supercell of the MoP_2 monolayer to determine the energetically favorable adsorption site of Na/K, considering sites S1 to S5 as marked in Fig. 4a. The adsorption energy is given by $E_{ad} = E_{MoP2+Na/K} - E_{MoP2} - E_{Na/K}$, where $E_{MoP2+Na/K}$ is the total energy of the MoP_2 monolayer with adsorbed Na/K atom and $E_{Na/K}$ is the total energy per atom in bulk Na/K. Negative E_{ad} avoids agglomeration of Na/K atoms (dendrite formation). According to the results in Fig. 4b, adsorption of Na/K is possible on top of the center of the Mo_2P_3 ring (S1 site), on top of Mo (S2 site), on top of P (S3 site), and on top of the P-P bond (S4 site), whereas Na/K on top of the Mo-P bond (S5 site) relaxes to the S2 site during the structure relaxation. The obtained values of E_{ad} and corresponding adsorption heights are reported in Table 2, demonstrating that the S2 site is energetically favorable. Furthermore, the charge redistributions between Na/K and the MoP_2 monolayer are shown in Fig. 4c–j for the S1–S4 sites, demonstrating that Na/K acts as charge donor. Bader charge analysis results in charge transfers of 0.85–0.89 electrons, see Table 2.

To estimate the charge-discharge rate, a key factor of an anode material, we study the diffusion barrier of Na/K in Fig. 5a, b. Figure 5c–f presents the obtained Na/K diffusion paths between neighboring S2 sites: S2 → S1 → S2 (path 1) and S2 → S1 → S4 → S1 → S2 (path 2). In the case

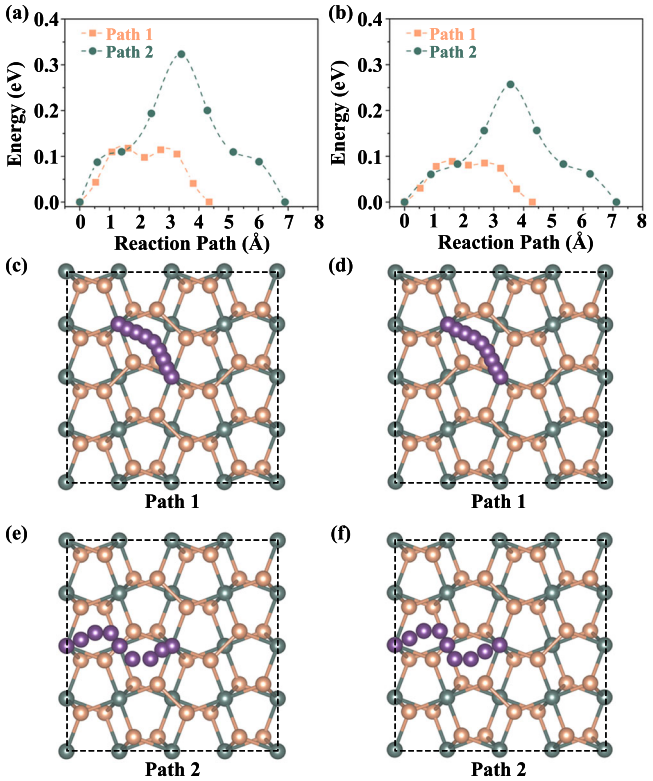

Fig. 5 | Diffusion. a Na and (**b**) K diffusion barriers on the MoP_2 monolayer. The diffusion paths are shown in (**c**, **e**) and (**d**, **f**), respectively.

of Na/K, we obtain for path 1 a diffusion barrier of 0.12/0.09 eV and for path 2 a diffusion barrier of 0.32/0.26 eV. Hence, path 1 is energetically favorable for both Na and K. The obtained Na/K diffusion barriers are comparable to those of blue phosphorene (0.11/0.09 eV)[37] and lower than those of Ti_2CP_2 (0.29/0.19 eV)[38], GeP_3 (0.27/0.29 eV)[39], AlP_3 (0.41/0.20 eV)[40], CoP (0.38/0.32 eV)[41], and MoN_2 (0.56/0.49 eV)[42]. A low diffusion barrier ensures mobility of Na/K and, consequently, a high charge-discharge rate.

To determine the specific capacity, another key factor of an anode material, we successively add Na/K atoms on both sides of the MoP_2 monolayer ($2 \times 2 \times 1$ supercell). The maximal adsorption is achieved when the adsorption energy $E_{ad}(m) = E_{MoP2(Na/K)m+1} - E_{MoP2(Na/K)m} - E_{Na/K}$ switches from negative to positive, where $E_{MoP2\ (Na/K)m}$ is the total energy when m Na/K atoms are adsorbed. It turns out that the MoP_2 monolayer can accommodate 32 Na and 29 K atoms, which corresponds to stoichiometries of MoP_2Na_2 and $MoP_2K_{1.81}$, respectively. Therefore, the specific capacity $C = mF/M$, where $F = 26801$ mA h mol^{-1} is the Faraday constant and $M = 158$ g mol^{-1} is the relative molecular mass of the MoP_2 monolayer, is found to be 339/308 mA h g^{-1} for Na/K. These values exceed those of the commercial graphite anode (284/273 mA h g^{-1})[12,13]. Compared with other two-dimensional anode materials, the value for Na exceeds those of Mo_2C (132 mA h g^{-1})[43], MoS_2 (146 mA h g^{-1})[44], Mo_2P (240 mA h g^{-1})[45], SnP_3 (253 mA h g^{-1})[46], and InP_3 (258 mA h g^{-1})[47]. The value for K exceeds those of Ti_3C_2 (192 mA h g^{-1})[48], CoP (208 mA h g^{-1})[41], GeS (256 mA h g^{-1})[49], and T-$NiSe_2$ (247 mA h g^{-1})[50].

We further study the stability of the structures with adsorbed Na/K atoms by calculating the formation energy of $MoP_2(Na/K)_m$ with respect to the MoP_2 monolayer and $MoP_2(Na_2/K_{1.81})$ as

$$E_f(m) = E_{MoP2Nam} - (mE_{MoP2Na2} + (2-m)E_{MoP2})/2$$

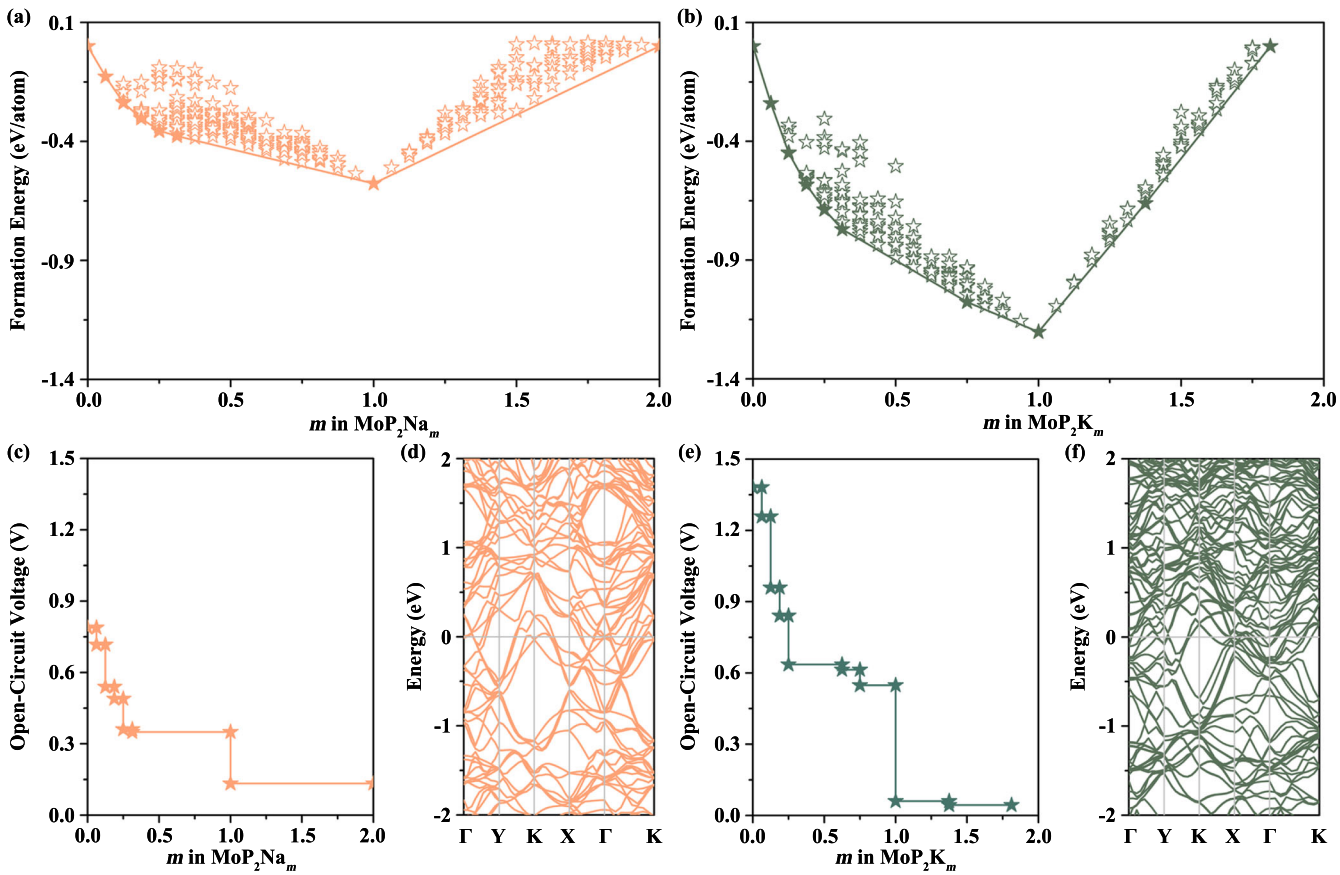

Fig. 6 | Adsorption. Formation energy as function of the (**a**) Na and (**b**) K coverage. Open-circuit voltage as function of the (**c**) Na and (**e**) K coverage (for the thermodynamically stable structures). Electronic band structures of (**d**) MoP_2Na_2 and (**f**) $MoP_2K_{1.81}$ (Fermi level = energy zero).

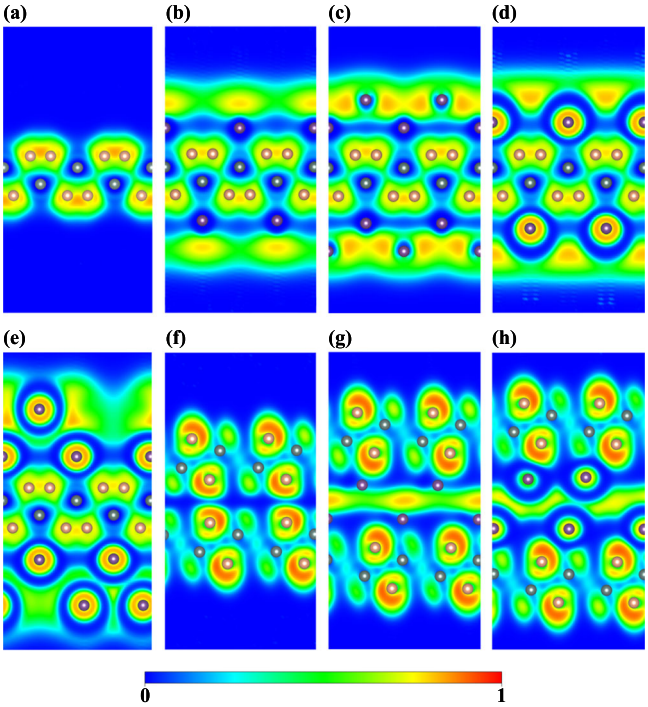

Fig. 7 | Localization. Electron localization function of the MoP_2 monolayer [(010) plane] (**a**) without adsorbed atoms, (**b**) with one layer of adsorbed Na atoms, (**c**) with maximal number of adsorbed Na atoms, (**d**) with one layer of adsorbed K atoms, and (**e**) with maximal number of adsorbed K atoms. Electron localization function of the MoP_2 bilayer [(010) plane] (**f**) without adsorbed atoms, (**g**) with maximal number of intercalated Na atoms, and (**h**) with maximal number of intercalated K atoms.

or

$$E_f(m) = E_{\mathrm{MoP2K}m} - (mE_{\mathrm{MoP2K1.81}} + (1.81 - m)E_{\mathrm{MoP2}})/1.81.$$

The results are shown in Fig. 6a, b, with the data points on the convex hull representing the thermodynamically stable structures. Stability is found for $m = 0.06$, 0.13, 0.19, 0.25, 0.31, 1.00, and 2.00 in the case of Na (Supplementary Fig. 1) and for $m = 0.06$, 0.13, 0.19, 0.25, 0.31, 0.75, 1.00, 1.38, and 1.81 in the case of K (Supplementary Fig. 2). The open-circuit voltage $-E_{ave}/e$, where e is the elementary charge, is calculated for the stable structures. According to Fig. 6c, e, it decreases from 0.79 V at $m = 0.06$ to 0.13 V at $m = 2.00$ in the case of Na, with an average of 0.48 V, and from 1.38 V at $m = 0.06$ to 0.04 V at $m = 1.81$ in the case of K, with an average of 0.70 V. The decreasing trends of the open-circuit voltage to low values at maximal adsorption imply that the working voltage of the battery (when the anode is coupled to the cathode) will increase to high values. The metallicity of the MoP_2 monolayer is preserved at maximal Na/K coverage (Fig. 6d, f), as required for the anode to operate.

The electron localization functions of the MoP_2 monolayer with different amounts of adsorbed Na/K atoms are shown in Fig. 7a–e. Bader charge analysis indicates in the case of one adsorbed layer that each Na/K atom donates 0.64/0.51 electrons to the MoP_2 monolayer. In the case of maximal adsorption each atom in the inner Na/K layer donates 0.11/0.19 electrons to the outer Na/K layer and 0.52/0.47 electrons to the MoP_2 monolayer. The charge accumulation in the outer Na/K layer, see Fig. 7c, e, prohibits further Na/K adsorption. As volume changes during the charge-discharge process introduce structural defects and, therefore, lead to capacity decay, we turn our attention to the MoP_2 bilayer and find that it can accommodate an intercalation of two layers of Na/K atoms with $E_{ave} = -0.33/-0.55$ eV. The intercalation enlarges the interlayer distance to 7.24/9.12 Å, corresponding to a volume expansion of 118%/176%, which is decisively smaller than that of black phosphorus (443% for Na_3P and

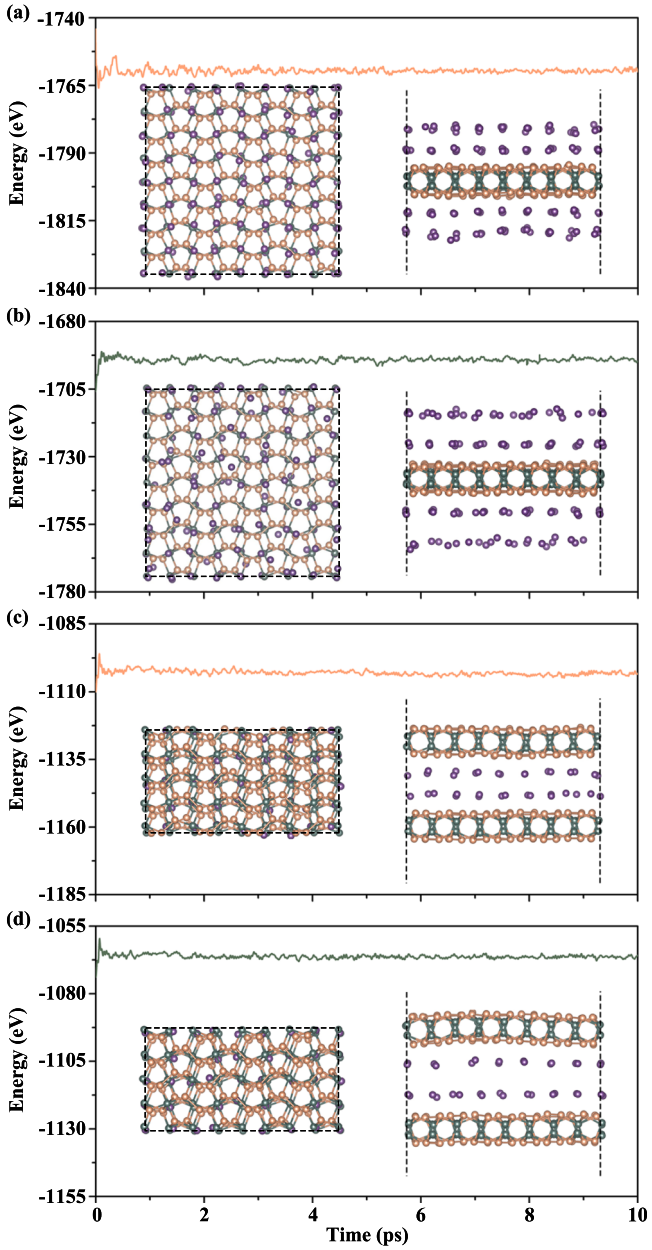

Fig. 8 | Adsorption and intercalation. Top and side views of the MoP_2 monolayer with maximal number of adsorbed (**a**) Na and (**b**) K atoms after the AIMD simulations at 300 K. Top and side views of the MoP_2 bilayer with two layers of intercalated (**c**) Na and (**d**) K atoms after the AIMD simulations at 300 K.

695% for K_3P)[19], for example. The electron localization functions of the MoP_2 bilayer without and with the intercalated atoms are shown in Fig. 7f–h. Each Na/K atom donates 0.44/0.43 electrons to the MoP_2 bilayer according to Bader charge analysis. AIMD simulations of the $MoP_2(Na_2/K_{1.81})$ monolayer and Na/K-intercalated MoP_2 bilayer, see Fig. 8, show no sign of structural collapse. The stacking of the MoP_2 bilayer shifts gradually to an AA pattern in the AIMD simulation while the interlayer distance increases to 7.31/9.28 Å for Na/K-intercalation, which still is a very small volume expansion of only 116%/180%. We finally investigate in Fig. 9a the Na specific capacity as a function of the number of MoP_2 layers (n). It turns out that always two layers of Na atoms can be accommodated, see Fig. 9b, corresponding to a stoichiometry of $MoP_2Na_{1+1/n}$. For bulk MoP_2Na ($n \to \infty$), see Fig. 9c, we find $E_{ave} = -0.34$ eV and a Na specific capacity of 170 mA h g^{-1}. The obtained interlayer distance of 7.45 Å corresponds to a volume expansion of 125%.

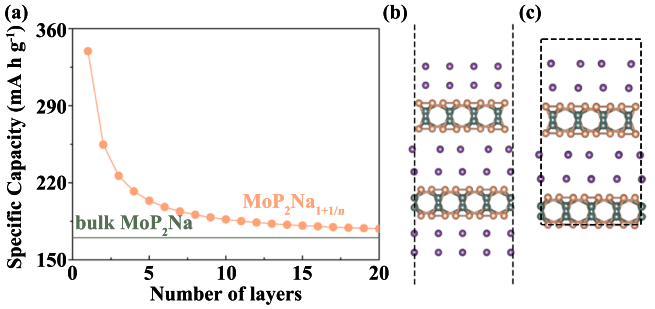

Fig. 9 | Adsorption and intercalation. a Na specific capacity as function of the number of MoP_2 layers. Side view of (**b**) the MoP_2 bilayer with maximal Na loading and (**c**) bulk MoP_2Na.

Our ab initio evolutionary search for metal phosphide monolayers points to the existence of a MoP_2 monolayer that is dynamically, thermally, and mechanically stable according to the calculated phonon spectrum, AIMD simulations at room and elevated temperatures, and the calculated elastic constants, respectively. We find that this MoP_2 monolayer provides excellent properties for application as anode material for NIBs/KIBs. Specifically, for Na it combines a high specific capacity of 339 mA h g^{-1}, a low diffusion barrier of 0.12 eV, and a low average open-circuit voltage of 0.48 V with a small volume expansion of only 125%.

Methods

We employ the USPEX[51–53] code to perform a global structure search for different Mo:P ratios, limited to a maximum of 16 atoms in the primitive unit cell. The population size is set to 100 and the number of generations is set to 50. We adopt density functional theory (Vienna Ab-initio Simulation Package[54]) to perform structural relaxations and electronic structure calculations with the exchange-correlation functionals of Perdew-Burke-Ernzerhof and Heyd-Scuseria-Ernzerhof, respectively, where the van der Waals interaction is taken into account by the DFT-D3 method[55] for the MoP_2 monolayer and by the optB88-vdW method[56] for the MoP_2 bilayer to achieve reliable results. The plane wave cutoff energy is set to 600 eV, the total energy is converged to 10^{-6} eV, and the atomic forces are converged to 10^{-3} eV/Å. A Monkhorst-Pack k-sampling with 0.015 Å^{-1} spacing is used. Each simulation cell contains a vacuum slab of at least 20 Å thickness. The Phonopy code is adopted to calculate the phonon band structures using a $4 \times 4 \times 1$ supercell of the MoP_2 monolayer[57]. Ab initio molecular dynamics (AIMD) simulations are carried out for 10 ps based on a canonical ensemble and a Nosé-Hoover temperature control[58]. They are conducted at 300, 1000, 1800, and 1900 K for a $4 \times 4 \times 1$ supercell of the MoP_2 monolayer and at 300 K for a $4 \times 2 \times 1$ supercell of the MoP_2 bilayer. A time step of 1 fs is used. The Na/K diffusion barriers and pathways are derived by means of the climbing-image nudged elastic band method[59].

Data availability

The data supporting the findings of this study are available within the article.

Received: 29 July 2023; Accepted: 15 February 2024;
Published online: 06 April 2024

References

1. Zubi, G., Dufo-López, R., Carvalho, M. & Pasaoglu, G. The Lithium-Ion Battery: State of the Art and Future Perspectives. *Renew. Sust. Energ. Rev.* **89**, 292–308 (2018).
2. Cano, Z. P. et al. Batteries and Fuel Cells for Emerging Electric Vehicle Markets. *Nat. Energy* **3**, 279–289 (2018).
3. Liang, Y. et al. A Review of Rechargeable Batteries for Portable Electronic Devices. *InfoMat.* **1**, 6–32 (2019).
4. Piątek, J., Afyon, S., Budnyak, T. M., Budnyk, S., Sipponen, M. H. & Slabon, A. Sustainable Li-Ion Batteries: Chemistry and Recycling. *Adv. Energy Mater.* **11**, 2003456 (2021).
5. Zhu, Z. et al. Rechargeable Batteries for Grid Scale Energy Storage. *Chem. Rev.* **122**, 16610–16751 (2022).
6. Kim, H., Kim, J. C., Bianchini, M., Seo, D.-H., Rodriguez-Garcia, J. & Ceder, G. Recent Progress and Perspective in Electrode Materials for K-Ion Batteries. *Adv. Energy Mater.* **8**, 1702384 (2018).
7. Vaalma, C., Buchholz, D., Weil, M. & Passerini, S. A Cost and Resource Analysis of Sodium-Ion Batteries. *Nat. Rev. Mater.* **3**, 18013 (2018).
8. Zhao, Y. et al. Recycling of Sodium-Ion Batteries. *Nat. Rev. Mater.* **8**, 623–634 (2023).
9. Sada, K., Darga, J. & Manthiram, A. Challenges and Prospects of Sodium-Ion and Potassium-Ion Batteries for Mass Production. *Adv. Energy Mater.* **13**, 2302321 (2023).
10. Olsson, E., Yu, J., Zhang, H., Cheng, H.-M. & Cai, Q. Atomic-Scale Design of Anode Materials for Alkali Metal (Li/Na/K)-Ion Batteries: Progress and Perspectives. *Adv. Energy Mater.* **12**, 2200662 (2022).
11. Kaskhedikar, N. A. & Maier, J. Lithium Storage in Carbon Nanostructures. *Adv. Mater.* **21**, 2664–2680 (2009).
12. Jian, Z., Luo, W. & Ji, X. Carbon Electrodes for K-Ion Batteries. *J. Am. Chem. Soc.* **137**, 11566–11569 (2015).
13. Xu, J. et al. Recent Progress in Graphite Intercalation Compounds for Rechargeable Metal (Li, Na, K, Al)-Ion Batteries. *Adv. Sci.* **4**, 1700146 (2017).
14. Mukherjee, S. & Singh, G. Two-Dimensional Anode Materials for Non-Lithium Metal-Ion Batteries. *ACS Appl. Energy Mater.* **2**, 932–955 (2019).
15. Zhao, Z., Yu, T., Zhang, S., Xu, H., Yang, G. & Liu, Y. Metallic P_3C Monolayer as Anode for Sodium-Ion. *Batteries, J. Mater. Chem. A* **7**, 405–411 (2019).
16. Wang, W., Meng, J., Hu, Y., Wang, J., Li, Q. & Yang, J. Thgraphene: A Novel Two-Dimensional Carbon Allotrope as a Potential Multifunctional Material for Electrochemical Water Splitting and Potassium-Ion Batteries. *J. Mater. Chem. A* **10**, 9848–9857 (2022).
17. Kumar, M. R. et al. Next Generation 2D Materials for Anodes in Battery Applications. *J. Power Sources* **556**, 232256 (2023).
18. Jin, H. et al. A Black Phosphorus-Graphite Anode for Li-/Na-/K-Ion Batteries. *Angew. Chem.* **132**, 2338–2342 (2020).
19. Zeng, L. et al. Phosphorus-Based Materials for High-Performance Alkaline Metal Ion Batteries: Progress and Prospect. *Small* **18**, 2201808 (2022).
20. Li, Q. et al. Advances in Metal Phosphides for Sodium-Ion Batteries. *SusMat* **1**, 359–392 (2021).
21. Zhao, X. et al. The Cutting-Edge Phosphorus-Rich Metal Phosphides for Energy Storage and Conversion. *Nano Today* **40**, 101245 (2021).
22. Winkler, B., Knorr, K., Hytha, M., Milman, V., Soto, V. & Avalos, M. Crystal Chemistry of Molybdenum Phosphides from Density Functional Theory Calculations. *J. Phys. Chem. Solids* **64**, 405–411 (2003).
23. Wu, T., Pi, M., Zhang, D. & Chen, S. Three-Dimensional Porous Structural MoP_2 Nanoparticles as a Novel and Superior Catalyst for Electrochemical Hydrogen Evolution. *J. Power Sources* **328**, 551–557 (2016).
24. Lou, H., Qiu, K. & Yang, G. Janus Mo_2P_3 Monolayer as an Electrocatalyst for Hydrogen Evolution. *ACS Appl. Mater. Interfaces* **13**, 57422–57429 (2021).
25. Laniel, D. et al. High-Pressure Polymeric Nitrogen Allotrope with the Black Phosphorus Structure. *Phys. Rev. Lett.* **124**, 216001 (2020).
26. Becke, A. D. & Edgecombe, K. E. A Simple Measure of Electron Localization in Atomic and Molecular Systems. *J. Chem. Phys.* **92**, 5397–5403 (1990).

27. Yang, L.-M. & Ganz, E. Adding a New Dimension to the Chemistry of Phosphorus and Arsenic. *Phys. Chem. Chem. Phys.* **18**, 17586–17591 (2016).
28. Cuan, J., Zhu, Z. & Tománek, D. Phase Coexistence and Metal-Insulator Transition in Few-Layer Phosphorene: A Computational Study. *Phys. Rev. Lett.* **113**, 046804 (2014).
29. Li, X. & Wang, Q. Prediction of a BeP_2 Monolayer with a Compression-Induced Dirac Semimetal State. *Phys. Rev. B* **97**, 085418 (2018).
30. Zheng, S., Yu, T., Lin, J., Lou, H., Xu, H. & Yang, G. FeP_3 Monolayer as a High-Efficiency Catalyst for Hydrogen Evolution Reaction. *J. Mater. Chem. A* **7**, 25665–25671 (2019).
31. Wang, L., Kutana, A., Zou, X. & Yakobson, B. I. Electro-Mechanical Anisotropy of Phosphorene. *Nanoscale* **7**, 9746–9751 (2015).
32. Sun, M. & Schwingenschlögl, U. Structure Prototype Outperforming MXenes in Stability and Performance in Metal-Ion Batteries: A High Throughput Study. *Adv. Energy Mater.* **11**, 2003633 (2021).
33. Peng, X., Wei, Q. & Copple, A. Strain-Engineered Direct-Indirect Band Gap Transition and Its Mechanism in Two-Dimensional Phosphorene. *Phys. Rev. B* **90**, 085402 (2014).
34. Xiong, S. & Cao, G. Molecular Dynamics Simulations of Mechanical Properties of Monolayer MoS_2. *Nanotechnology* **26**, 185705 (2015).
35. Jalil, A., Zhuo, Z., Sun, Z., Wu, F., Wang, C. & Wu, X. A Phosphorene-Like InP_3 Monolayer: Structure, Stability, and Catalytic Properties Toward the Hydrogen Evolution Reaction. *J. Mater. Chem. A* **8**, 1307–1314 (2020).
36. Lu, N. et al. CaP_3: A New Two-Dimensional Functional Material with Desirable Band Gap and Ultrahigh Carrier Mobility. *J. Phys. Chem. Lett.* **9**, 1728–1733 (2018).
37. Mukherjee, S., Kavalsky, L. & Singh, C. V. Ultrahigh Storage and Fast Diffusion of Na and K in Blue Phosphorene Anodes. *ACS Appl. Mater. Interfaces* **10**, 8630–8639 (2018).
38. Zhu, J. & Schwingenschlögl, U. P and Si Functionalized MXenes for Meta-Ion Battery Applications. *2D Mater.* **4**, 025073 (2017).
39. Deng, X., Chen, X., Huang, Y., Xiao, B. & Du, H. Two-Dimensional GeP_3 as a High Capacity Anode Material for Non-Lithium-Ion Batteries. *J. Phys. Chem. C* **123**, 4721–4728 (2019).
40. Wan, M., Zhang, Z., Peng, Y., Zhao, S. & Zhou, N. Graphene-Like AlP_3 Monolayer: A High-Performance Anode Material for Li/Na/K-Ion Batteries. *J. Solid State Chem*. **327**, 124284 (2023).
41. Banerjee, S., Narwal, A., Reddy, S. & Yamijala, K. S. S. R. K. C. Promising Anode Materials for Alkali Metal Ion Batteries: A Case Study on Cobalt Anti-MXenes. *Phys. Chem. Chem. Phys.* **25**, 11789–11804 (2023).
42. Zhang, X. et al. Theoretical Prediction of MoN_2 Monolayer as a High Capacity Electrode Material for Metal Ion Batteries. *J. Mater. Chem. A* **4**, 15224–15231 (2016).
43. Sun, Q., Dai, Y., Ma, Y., Jing, T., Wei, W. & Huang, B. Ab Initio Prediction and Characterization of Mo_2C Monolayer as Anodes for Lithium-Ion and Sodium-Ion Batteries. *J. Phys. Chem. Lett.* **7**, 937–943 (2016).
44. Mortazavi, M. et al. Ab initio Characterization of Layered MoS_2 as Anode for Sodium-Ion Batteries. *J. Power Sources* **268**, 279–286 (2014).
45. Mortazavi, B., Shahrokhi, M., Makaremi, M. & Rabczuk, T. Theoretical Realization of Mo_2P: A novel Stable 2D Material with Superionic Conductivity and Attractive Optical Properties. *Appl. Mater. Today* **9**, 292–299 (2017).
46. Liu, C.-S., Yang, X.-L., Liu, J. & Ye, X.-J. Theoretical Prediction of Two-Dimensional SnP_3 as a Promising Anode Material for Na-Ion Batteries. *ACS Appl. Energy Mater* **1**, 3850–3859 (2018).
47. Liu, J., Liu, C.-S., Ye, X.-J. & Yan, X.-H. Monolayer InP_3 as a Reversible Anode Material for Ultrafast Charging Lithium- and Sodium-Ion Batteries: A Theoretical Study. *J. Mater. Chem. A* **6**, 3634–3641 (2018).
48. Er, D., Li, J., Naguib, M., Gogotsi, Y. & Shenoy, V. B. Ti_3C_2 MXene as a High Capacity Electrode Material for Metal (Li, Na, K, Ca) Ion Batteries. *ACS Appl. Mater. Interfaces* **6**, 11173–11179 (2014).
49. Li, F., Qu, Y. & Zhao, M. Germanium Sulfide Nanosheet: A Universal Anode Material for Alkali Metal Ion. *Batteries, J. Mater. Chem. A* **4**, 8905–8912 (2016).
50. Shen, Y., Liu, J., Li, X. & Wang, Q. Two-Dimensional T-$NiSe_2$ as a Promising Anode Material for Potassium-Ion Batteries with Low Average Voltage, High Ionic Conductivity, and Superior Carrier Mobility. *ACS Appl. Mater. Interfaces* **11**, 35661–35666 (2019).
51. Oganov, A. R. & Glass, C. W. Crystal Structure Prediction Using Ab Initio Evolutionary Techniques: Principles and Applications. *J. Chem. Phys.* **124**, 244704 (2006).
52. Oganov, A. R., Lyakhov, A. O. & Valle, M. How Evolutionary Crystal Structure Prediction Works and Why. *Acc. Chem. Res.* **44**, 227–237 (2011).
53. Lyakhov, A. O., Oganov, A. R., Stokes, H. T. & Zhu, Q. New Developments in Evolutionary Structure Prediction Algorithm USPEX. *Comput. Phys. Commun.* **184**, 1172–1182 (2013).
54. Kresse, G. & Joubert, D. From Ultrasoft Pseudopotentials to the Projector Augmented-Wave Method. *Phys. Rev. B* **59**, 1758–1775 (1999).
55. Grimme, S., Antony, J., Ehrlich, S. & Krieg, H. A Consistent and Accurate *Ab Inito* Parametrization of Density Functional Dispersion Correction (DFT-D) for the 94 Elements H-Pu. *J. Chem. Phys.* **132**, 154104 (2010).
56. Thonhauser, T., Cooper, V. R., Li, S., Puzder, A., Hyldgaard, P. & Langreth, D. C. Van der Waals Density Functional: Self-Consistent Potential and the Nature of the Van der Waals. *Phys. Rev. B* **76**, 125112 (2007).
57. Togo, A. & Tanaka, I. First Principles Phonon Calculations in Materials Science. *Scr. Mater.* **108**, 1–5 (2015).
58. Martyna, G. J., Klein, M. L. & Tuckerman, M. Nosé-Hoover Chains: The Canonical Ensemble Via Continuous Dynamics. *J. Chem. Phys*. **97**, 2635–2643 (1992).
59. Henkelman, G., Uberuaga, B. P. & Jónsson, H. A Climbing Image Nudged Elastic Band Method for Finding Saddle Points and Minimum Energy Paths. *J. Chem. Phys*. **113**, 9901–9904 (2000).

Acknowledgements

The research reported in this publication was supported by funding from King Abdullah University of Science and Technology (KAUST).

Author contributions

J.J. performed the calculations. All authors contributed to the data analysis and manuscript writing.

Competing interests

The authors declare no competing interests.

Additional information

Supplementary information The online version contains supplementary material available at https://doi.org/10.1038/s41699-024-00453-0.

Correspondence and requests for materials should be addressed to Udo Schwingenschlögl.